

# FLUIDODYNAMIC ANALYSIS OF LOW REYNOLDS NUMBER FLOWS

Nicola Verde<sup>1</sup>, Federico Capoluongo<sup>1</sup>, Pietro Catalano<sup>2</sup>, Giuseppe Pezzella<sup>1</sup> & Antonio Viviani<sup>1</sup>

Università della Campania "Luigi Vanvitelli", Dipartimento di Ingegneria. Via Roma 29, I-81031. Aversa (CE). Italy.
 Laboratorio di Meccanica dei Fluidi, Centro Italiano Ricerche Aerospaziali - CIRA, Capua (CE), Italy.

#### **Abstract**

This paper deals with the fluid dynamic analysis of subsonic uncompressible and compressible flows characterized by low Reynolds numbers over several wing sections, carried out with panel method tools such as XFoil, and advanced high fidelity Computational Fluid Dynamics tools, like ANSYS-FLUENT and SU2. The primary goal is to investigate the complex flow phenomena of laminar-to-turbulent transition and formation and separation of laminar bubbles with the aim to assess aerodynamic performances of several airfoils. Special attention was devoted to the intricacies associated with low-Reynolds number flows, characteristic of flight conditions in the Martian atmosphere under subsonic speed. Reynolds-Averaged Navier-Stokes simulations are carried out at Reynolds numbers ranging from  $11\times10^3$  to  $60\times10^3$  and for different angles of attack. These flow conditions are considered being representative of typical free-stream conditions for a fixed wing drone for Mars flying exploration. Flow turbulence is addressed by means of the Shear-Stress Transport  $\gamma$ -Re $_\theta$  model to enhances the accuracy of predictions for flow patterns and characteristics at low Reynolds flow conditions. A detailed description of the flowfield past the investigated airfoils with the corresponding aerodynamic force and moments coefficients is provided in the paper.

Keywords: CFD, Low-Reynolds flow, Turbulence, Laminar-to-turbulent transition, laminar separation bubbles

#### 1 Introduction

The aim of this research effort is to undertake a thorough steady state Computational Fluid Dynamics (CFD) analysis of the flowfield that takes place past several wing sections at low Reynolds number conditions with the aim to assess their aerodynamic performances. Numerical simulations are performed in different environments, encompassing ANSYS-FLUENT®, SU2, and XFoil [1]. Flowfield investigations are carried out by means of Reynolds-Averaged Navier-Stokes (RANS) simulations with the focus on both subsonic uncompressible and compressible flows at Reynolds numbers ranging from  $11\times10^3$  to  $60\times10^3$  and for different angles of attack,  $\alpha$ . These flow conditions are considered being representative of typical free-stream conditions for a fixed wing Unmanned Aerial Vehicle (UAV) for Mars flying exploration [2] [3] [4]. In this framework, the research investigation encompasses several wing sections, including commercially available ones, such as NACA0012-34, Eppler 387, SD7003, and ISHII, and proprietary optimized airfoils, obtained by means of in-house design tools [2] [3]. Particular care is addressed in modelling turbulence levels within the CFD simulations because of their influence on transition position and separation bubble extent. With this in mind, CFD simulations are carried out with both fully turbulent and transitional flow models. Fully turbulent investigations are performed with Spalart-Allmaras (SA) and Shear-Stress Transport (SST) k-ω models, while for transitional flow conditions the selected turbulence model is the SST y-Ree model, a choice that enhances the accuracy of predictions for flow patterns and characteristics at low Reynolds flow conditions [5]. The overarching objective is not only to uncover insights into the aerodynamic behavior of these wing profiles but also to shed light on the intricate interplay of fluid forces and boundary layer dynamics, particularly in the challenging domain of low Reynolds numbers [6]. Most CFD analyses are numerical rebuilding of several Wind Tunnel (WT) tests available in literature [7]. Therefore, the accuracy of the numerical data provided hereinafter through different methods and models is evaluated by means of CFD and WT data comparisons for force and moment coefficients. In doing this, the effect of free-stream turbulence level on the laminar separation bubbles extent, the transition position, and then on the aerodynamics of airfoil is verified in detail.

Variables of interest encompassed the transition position, the augmentation in turbulent kinetic energy production within the separation zone within the recirculation region, the progression of the bubble concerning the angle of incidence and turbulence levels, potential ruptures of the bubble at high incidences, and the subsequent ramifications on stall characteristics. A meticulous examination was undertaken on methods for analyzing laminar boundary layer buckling to address laminar separation bubbles. Meticulous modelling of turbulent kinetic energy production in the recirculation region was imperative for ensuring the accurate reproduction of pressure recovery and bubble characteristics [8].

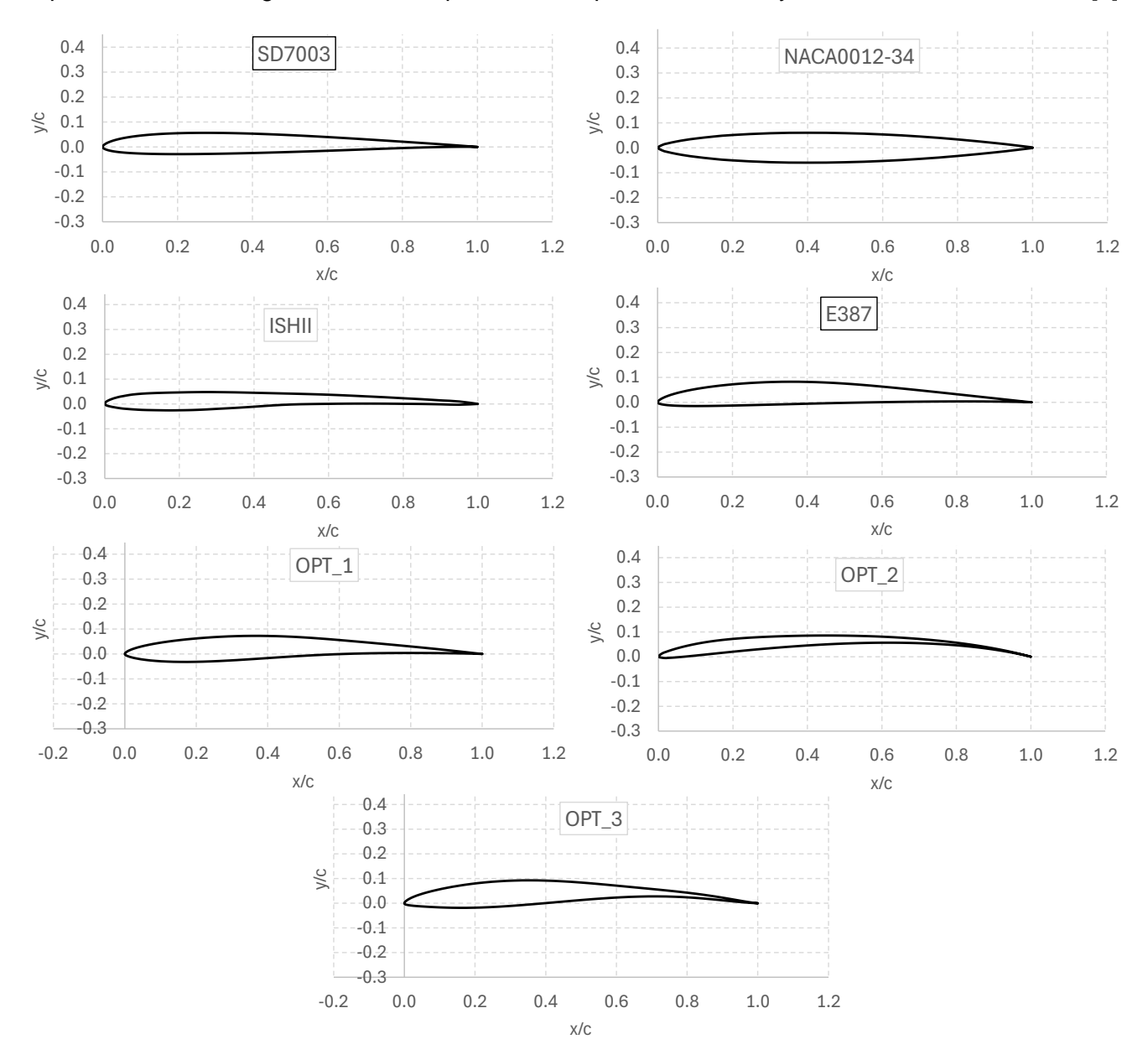


Figure 1 – Investigated airfoils.

Consequently, after conducting such CFD analyses, a comprehensive database was developed to extract fundamental information regarding turbulence level conditions of free-stream flow. Recall that this information plays a pivotal role while setting RANS simulations in order to address reliable flowfield solution. As a result, gathering all the results provided by numerical flowfield investigations a MATLAB® tool is developed with the capability to provide, based on Mach and Reynolds number conditions, together with the profile features, the levels of turbulent kinetic energy and the specific dissipation rate to be considered in free-stream flow conditions.

# 2 Investigated Airfoils

Seven airfoils were investigated in the present research work. They are summarized in Figure 1 and Table 1 where their geometrical characteristics are also provided.

| AIRFOIL      | MAX THICKNESS  | MAX CAMBER     |
|--------------|----------------|----------------|
| SD7003       | 8.5% @ 24.4% c | 1.2% @ 38.3% c |
| NACA 0012-34 | 1.2% @ 40% c   | 0% @ 0% с      |
| ISHII        | 7.1% @ 25% c   | 2.3% @ 62% c   |
| 0EPPLER 387  | 9.1% @ 31.1% c | 3.2% @ 44.8% c |
| OPT_1        | 9.6% @ 26% c   | 3.4% @ 44% c   |
| OPT_2        | 5.1% @ 18% c   | 7.1% @ 54% c   |
| OPT_3        | 9.8% @ 31% c   | 2.7% @ 81% c   |

Table 1 Airfoils characteristics

The Selig Donovan 7003 airfoil (SD7003) is characterized by a unique combination of high lift, low drag, and stable behavior at low speeds.

The NACA0012-34 airfoil represents a specific variant within the broader airfoil system developed by the National Advisory Committee on Aeronautics (NACA).

The ISHII profile is known for its efficiency and stability. In particular, it draws attention to specific events such as the formation of laminar bubbles and separations, especially on the underside, under conditions of low Angle of Attack (AoA).

The E387 airfoil, developed by Eppler, is an aerodynamic profile known for its excellent characteristics in terms of aerodynamic lift, drag and flow control for laminar flow conditions. The inclusion of this diverse set of airfoils enables a comprehensive analysis of aerodynamic performance across various flight conditions and speeds. Each wing section possesses unique characteristics, contributing to an integrated approach for understanding aerodynamic behavior in specific scenarios, including the challenges posed by low Reynolds number flows. The selection of above such different wing sections aims to provide a thorough overview of flow dynamics and aerodynamic performance expected to be particularly interesting for Martian exploration missions [9] [10].

Finally, due to the extensive presence of experimental and numerical data in the literature regarding Eppler 387 and considering its distinct features in scenarios like low Reynolds flows, an additional analysis was conducted on three airfoils, namely OPT\_1, OPT\_2, and OPT\_3 [11]. They are derived through design optimization activities carried out by the aerodynamic research group at the Department of Engineering of the University of Campania, starting from the E387 airfoil, with the aim at maximizing their lift-to-drag (L/D) ratios for low Reynolds flow conditions [2] [3].

#### 3 Aerodynamics of Low-Reynolds Number Flows

The upper threshold for the low Reynolds number regime is generally considered to be around 2×10<sup>5</sup> [9]. Below this limit, there is a notable decline in aerodynamic efficiency attributed to increased body drag, primarily due to the presence of laminar separations. The exploration of low-Reynolds number flows has gained significant attention, particularly driven by the aerospace industry interest in UAVs and Micro-Aerial Vehicles (MAVs). UAV wings typically operate with a Reynolds number ranging from 10<sup>4</sup> to 10<sup>5</sup>. In this range, the flow often experiences laminar separation due to the inability to sustain strong adverse pressure gradients.

At these Reynolds numbers, perturbations within the laminar region are amplified, leading to the transition to the turbulent regime. The turbulence that develops within the recirculating region enhances momentum transport, causing the flow to stall. Therefore, this phenomenon is critical in low Reynolds number flows and has a detrimental impact on aircraft performance. It results in an increase in resistance due to pressure (i.e., form drag) because of the decrease in suction on the airfoil leeside determine a subsequently reduction in pressure recovery. Additionally, frictional resistance rises due to increased turbulent momentum. When turbulent transport is insufficient to close the separated bubble, the flow fails to reattach, and the separated region extends to the trailing edge. This results in a loss of lift, increased drag, and hysteresis effects on force coefficients with changes in the AoA. Generally speaking, in this framework three flow phenomena, namely laminar separation, transition from laminar-to-turbulent, and interaction with turbulent flow complexity, are particularly important.

Recall that laminar separation manifests when a laminar flow encounters a curved surface or experiences a discontinuity in the flow geometry. In such scenarios, the flow may detach from the surface, giving rise to a recirculation or vorticity zone.

Further, laminar separation is commonly linked to notable pressure gradients or abrupt alterations in flow geometry. It has the potential to influence the stability of laminar flow and contribute to the development of turbulent structures.

The laminar-to-turbulent transition is a dynamic process in which an initially laminar flow undergoes instability and transforms into a turbulent state. This shift can be influenced by factors like elevated flow velocity or disturbances in the geometric configuration. A comprehensive understanding of the transition is vital, as flow behavior can markedly differ between laminar and turbulent regimes. Prediction of the transition often involves the use of the Reynolds number.

Finally, for what concerns the interaction with turbulent flow complexity, it is worth noting that within the turbulent regime, the occurrence of laminar separations and the transition from laminar to turbulent states introduces spatial and temporal intricacies to the flow. Laminar separation influences the creation of turbulent structures, and the transition marks a pivotal moment in altering the overall flow behavior.

In summary, when analyzing complex flows that encompass phenomena like laminar separations and transitions from laminar to turbulent states, it is essential to account for their interaction with the complexities of motion scales and variations in time and space. A detailed description of flowfield phenomena that take place at low Reynolds number flow conditions can be found in Reff. [6] [2] [3].

#### 4 Numerical setup

The findings presented in this research effort are derived using numerical methods rooted in the RANS equations. These methods entail the spatial and temporal averaging of the quantities of interest, respectively.

In RANS simulations, a time average is employed on the Navier-Stokes equations to achieve a more stable and simplified depiction of the flow compared to Large Eddy Simulation (LES). LES is an advanced CFD approach that directly simulates large turbulent structures, offering a detailed representation of complex flows but at the expense of higher computational efforts. Consequently, RANS is frequently chosen as a valid alternate when there is a need for a balance between accuracy and computational costs.

#### 4.1 Turbulence and transition models

The  $\kappa$ - $\omega$ - $\gamma$ -Re $_{\odot}$  turbulence model is employed. This advanced formulation is meticulously crafted to capture turbulence behavior with precision and efficiency in fluid flows. Its structural foundation rests upon a system of partial differential equations, modelling the spatiotemporal evolution of pivotal turbulent quantities. The model encompasses three primary variables:  $\kappa$  (i.e., turbulent kinetic energy),  $\omega$  (i.e., specific dissipation rate of k), and  $\gamma$  that is an additional variable associated with turbulence production. The introduction of  $\gamma$  serves to model turbulence production in regions characterized by strong velocity gradients.

The  $Re_{\Theta}$  component, integrated into the model, allows managing the transition from laminar to turbulent flows. This component is especially critical in flows crossing the transition zone, thus allowing the model to dynamically adapt to the varying flow conditions.

In summary, the overall structure of this mathematical model amalgamates the description of turbulent energy with detailed insights into dissipation and turbulent production, complemented by a transition management mechanism. Consequently, it furnishes a comprehensive and accurate representation of turbulence in complex flow conditions.

In the  $\kappa$ - $\omega$ - $\gamma$ -Re $_{\odot}$  model, the effect of turbulence is represented as an increase in viscosity, which in turn is seen as the sum of two contributions, namely laminar viscosity  $\mu$  and turbulent viscosity  $\mu_t$ . Turbulent viscosity is calculated through the Menter's SST turbulence model [12] [13]. Laminar viscosity introduces two transport equations: one for turbulent kinetic energy (k), see Eq. (1), and one for the dissipation rate ( $\omega$ ), see Eq. (2).

The laminar-to-turbulent transition is taken into account using the  $\gamma$ -Re $_{\theta}$  model, introducing Eq. (3) and Eq. (4) for intermittency,  $\gamma$ , and the Reynolds momentum thickness, Re $_{\theta}$ , respectively [13].

$$\frac{\partial}{\partial x_i}(\rho k u_i) = \frac{\partial}{\partial x_j} \left( \left( \mu_{+} \frac{\mu_t}{\sigma_k} \right) \frac{\partial k}{\partial x_j} \right) + G_k^* - Y_k^* + S_k^*$$
(1)

$$\frac{\partial}{\partial x_j} \left( \rho \omega u_j \right) = \frac{\partial}{\partial x_j} \left( \left( \mu_{+ \frac{\mu_t}{\sigma_\omega}} \right) \frac{\partial \omega}{\partial x_j} \right) + G_\omega^{\square} - Y_\omega^{\square} + S_\omega^{\square}$$
 (2)

$$\frac{\partial \left(\rho u_{j} \gamma\right)}{\partial x_{j}} = P_{\gamma 1} - E_{\gamma 1} + P_{\gamma 2} - E_{\gamma 2} + \frac{\partial}{\partial x_{j}} \left[ \left(\mu_{+} \frac{\mu_{t}}{\sigma_{\gamma}}\right) \frac{\partial \gamma}{\partial x_{j}} \right] \tag{3}$$

$$\frac{\partial \left(\rho u_j \widetilde{\operatorname{Re}}_{\theta t}\right)}{\partial x_i} = P_{\theta t} + \frac{\partial}{\partial x_i} \left[ \sigma_{\theta t} (\mu + \mu_t) \frac{\partial \widetilde{\operatorname{Re}}_{\theta t}}{\partial x_i} \right] \tag{4}$$

Equation have been adjusted with compared to those of Menter et al. in order to improve the predictions of the separate flow transition.

# 4.2 Numerical tools

Flowfield numerical investigations are carried out with panel method tools, such as XFoil, and advanced high fidelity CFD tools, like ANSYS-FLUENT and SU2. It is worth noting that, all CFD computations are carried out with the same grid, of course.

XFoil is an interactive tool for the design and analysis of subsonic airfoil profiles. It provides a quicker albeit less precise method for obtaining results and served as a valuable tool to obtain initial insights into the performance of the analyzed profiles, which were subsequently subjected to more detailed scrutiny using other solvers with higher precision. XFoil offers various functionalities, including viscous airfoil analysis, examination of separation bubbles, and the computation of lift, drag, and pitching moment coefficients. While XFoil provided a valuable preliminary step in the CFD analysis of this research work, it is crucial to acknowledge the importance of comparing its results with those obtained from other solvers such as ANSYS-FLUENT and SU2. Although these solvers demand more computational time, they offer enhanced accuracy and the ability to replicate results and phenomena that may not be achievable with XFoil.

ANSYS-FLUENT is a comprehensive CFD software that enables modelling and analysis of fluid behavior in various contexts and applications. With its advanced physical modelling capabilities, this tool is widely used for fluid flow simulation with a wide range of physical models, also including accurate turbulence modelling.

SU2 is an open-source computational analysis and optimization software with a focus on aerodynamic performance. It stands out as a freely available tool, and its programming code is crafted in C++. SU2 primary application lies in the analysis of aerodynamic performance achieved by solving partial differential equations. Additionally, SU2 encompasses modules designed for the optimization of profiles. Key attributes of SU2 include the robustness of results obtained through RANS simulations, accelerated simulation convergence through multi-griding and preconditioning operations, and the capability to execute parallel calculations using Message Passing Interface (MPI). For all the analyzed airfoils, a two-dimensional C-grid was created with a height and length of 60 chord lengths.

In the ANSYS-FLUENT environment, efforts were made to keep the settings consistent across all analyzed profiles whenever possible. Only parameters relevant to variations in Mach, Reynolds, and free-stream turbulence conditions are modified. Special attention was given to configuring the turbulence and transition model for each airfoil under investigation. For the incompressible simulations, the Semi-Implicit Method for Pressure-Linked Equations with Consistent (SIMPLEC) corrections for the pressure-velocity coupling method is employed. This method utilizes a relationship between the velocity and pressure corrections to ensure mass conservation and derive the pressure field. It differs from the SIMPLE algorithm in the expression used for flow correction on the face. The adoption of this modified correction equation aims to expedite convergence in situations where the pressure-velocity

coupling constraint poses a significant challenge to achieving a solution.

For compressible simulations, an implicit formulation with the Roe Flux-Difference Splitting (Roe-FDS) method was employed. The flow vector is evaluated using an upwind standard, acknowledging that the flow vector contains characteristic information propagating through the domain based on the eigenvalues of the system. The Roe-FDS method divides the flow vector into parts, each carrying information moving in a specific direction (characteristic information). In its current form, the flow discretization involves a second-order central difference plus an added matrix dissipation term which induces upwinding of convective variables, pressure, and velocity in supersonic flows and also provides the pressure-velocity coupling, necessary for stability and efficient convergence in low-velocity and incompressible flows. Concerning the discretization of equation terms, second order discretization were applied using an upwind method. Once the method for solving the equations was established, the next steps involved setting output parameters to indicate which coefficients to obtain as results (lift and drag). After initialization, the simulation was initiated.

#### 5 Flowfield Results

Numerical investigations began with the goal of choosing the most reliable turbulence model to be considered in the CFD numerical calculations performed in this research work. With this in mind, several turbulence models are considered to address the flowfield that takes place past a SD7003 airfoil at  $M_{\infty}{=}0.15$  and  $Re_{\infty}{=}60{\times}10^3$  and results compared with those of a LES computation [6]. The investigated turbulence models were the SA model (i.e., run with the fully turbulent assumption) and the k- $\omega$ - $\gamma$  model. The numerical results of this model trade-off are compared in terms of pressure coefficient distribution in Figure 2.

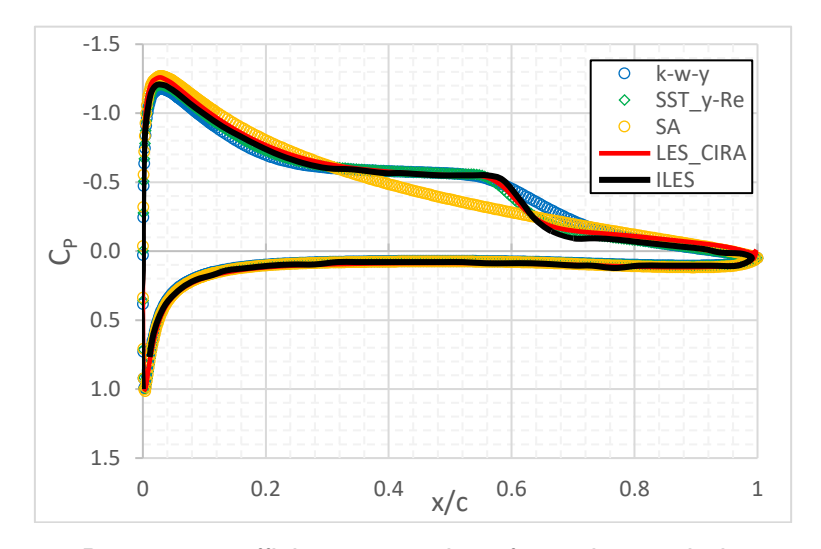


Figure 2 – Pressure coefficient comparison for various turbulence models.

As one can see, the  $\kappa$ - $\omega$ - $\gamma$ -Re $_{\odot}$  turbulence model compare rather well with LES results and so such model was assumed reliable and effective to perform all the CFD flowfield investigations summarized in the CFD test matrix reported in Table 2.

| Airfoils    | Reynolds No.       | Mach No. |
|-------------|--------------------|----------|
| SD7003      | 60×10 <sup>3</sup> | 0.15     |
| NACA0012-34 | 11×10 <sup>3</sup> | 0.20     |
| NACA0012-34 | 11×10 <sup>3</sup> | 0.60     |
| ISHII       | 23×10 <sup>3</sup> | 0.20     |
| EPPLER 387  | 60×10 <sup>3</sup> | 0.05     |
| OPT_1       | $34 \times 10^{3}$ | 0.05     |
| OPT_2       | $34 \times 10^{3}$ | 0.05     |
| OPT_3       | 45×10 <sup>3</sup> | 0.15     |

Table 2 CFD Test Matrix

### 5.1 SD7003 airfoil at Re $\infty$ =60×10<sup>3</sup> and M $\infty$ =0.15

The aerodynamic performance of the SD7003 airfoil at  $M_{\infty}$ =0.15 and  $Re_{\infty}$ =60x10³ is shown in Figure 3, where the lift coefficient versus  $\alpha$  is provided. In this figure, results comparison among XFoil, CFD simulations with ANSYS-FLUENT and SU2, LES investigations, and some experimental data is also reported. Note that XFoil results rely on free flow transition computation. As one can see, CFD and experimental data compare rather well, thus confirming the reliability of the  $\kappa$ - $\omega$ - $\gamma$ - $Re_{\Theta}$  model in representing aerodynamic characteristics at low Re conditions.

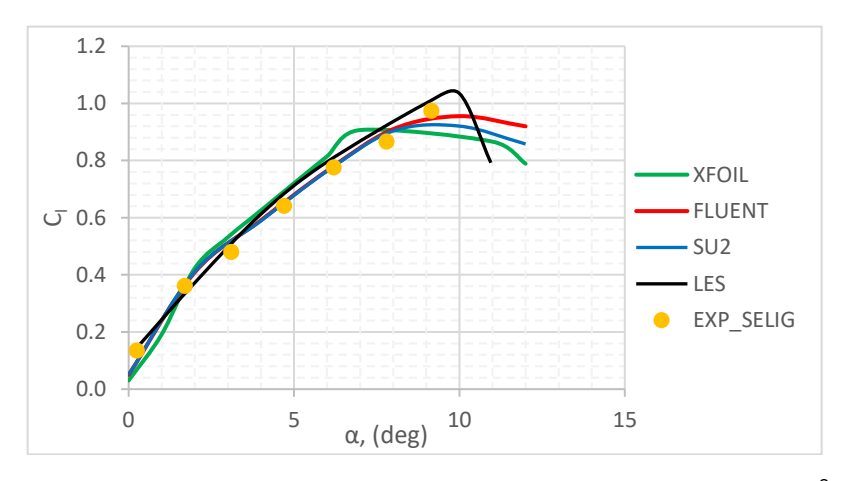


Figure 3 –  $C_1$  vs  $\alpha$ . SD7003 airfoil at  $M_{\infty}$ =0.15 and  $Re_{\infty}$ =60x10<sup>3</sup>

The local skin friction coefficient (CF) versus x/c at  $\alpha$ =4 deg are provided in Figure 4 for both RANS and LES computations.

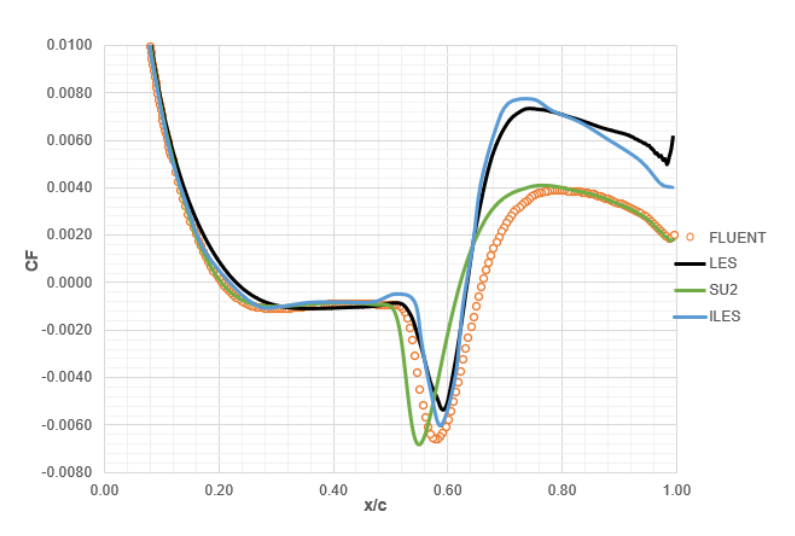


Figure 4 – SD7003. CF at  $\alpha$ =4°,  $M_{\infty}$ =0.15 and  $Re_{\infty}$ =60x10<sup>3</sup>

The evolution of CF together with the analysis of turbulent viscosity contours are of paramount importance in assessing airfoil aerodynamics. In fact, they help identifying separation and flow transition zones, crucial for understanding airfoil aerodynamics. For instance, Figure 4 points out that at  $\alpha$ =4 deg a separation bubble takes place on the leeside of the SD7003 airfoil. Laminar flow separates (i.e., CF $\leq$ 0) starting at about 20% of chord (x/c=0.20), reattaches (i.e., CF $\geq$ 0) close to x/c=0.60, and becomes turbulent along the way, as highlighted by eddy viscosity contours. The complete evolution of flow separation and reattachment points while  $\alpha$  ranges from 0 deg to 10 deg (i.e., before stall conditions, see Figure 3) is shown in Figure 5. It compares both RANS and LES results and clearly illustrates how changes in AoA strongly influence the location of these critical points, as expected. Additionally, Figure 5 also reveals small differences between RANS simulations and LES data at higher angles of attack. Finally, the evolution of the bubble with AoA is clearly shown. The bubble moves

towards the leading edge as AoA increases.

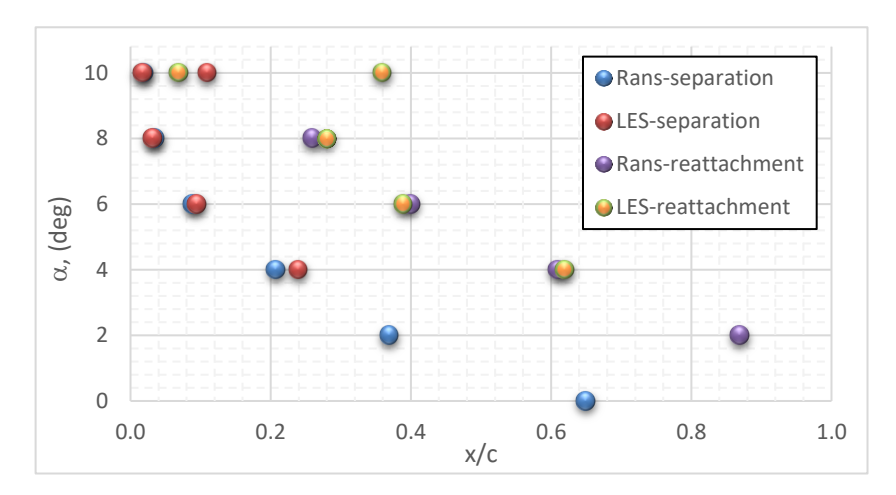


Figure 5 – SD7003. Separation and reattachment points at  $0^{\circ} \le \alpha \le 10^{\circ}$  for  $M_{\infty} = 0.15$  and  $Re_{\infty} = 60 \times 10^{3}$ 

# 5.2 NACA0012-34 airfoil at Re $_{\infty}$ =11×10<sup>3</sup> and M $_{\infty}$ =0.20

The aerodynamics of NACA0012-34 airfoil at  $M_{\infty}$ =0.20 and  $Re_{\infty}$ =11x10³ is shown in Figure 6, where lift coefficients provided by XFoil and ANSYS-FLUENT are compared with WT experimental data [14]. As shown, at these flow conditions the XFoil solver struggles to accurately reproduce experimental data, since its results rely on free transition simulation.

On the other hand, results of ANSYS-FLUENT simulations show favorable correspondence, accurately replicating the aerodynamic stall phenomenon and qualitative trends in the  $C_L$  versus  $C_D$  graph, summarized in Figure 10.

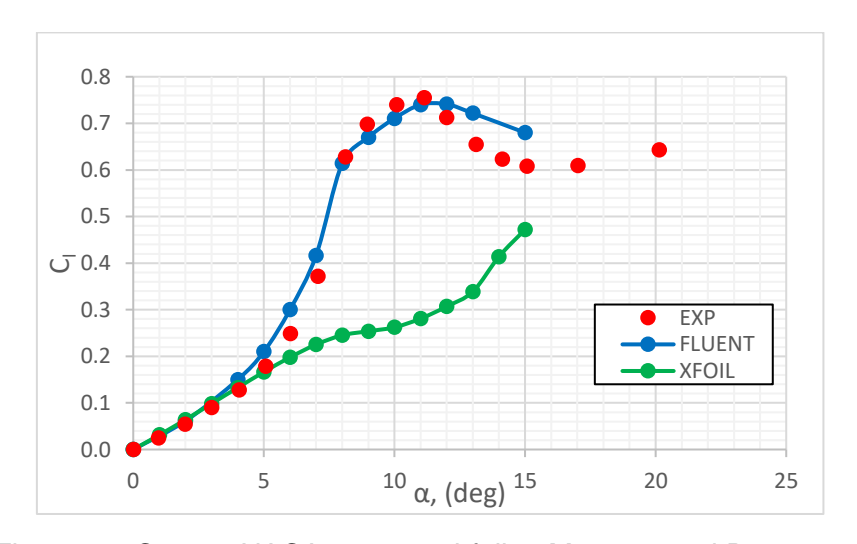


Figure 6 –  $C_1$  vs  $\alpha$ . NACA0012-34 airfoil at  $M_{\infty}$ =0.20 and  $Re_{\infty}$ =11x10<sup>3</sup>

Numerical results for the skin friction coefficient (CF) are shown in Figure 7 for both  $\alpha$ =7 deg and 10 deg. Extensions of the laminar separation bubble in these two flow conditions are clearly recognizable from the zone of CF negative values.

At  $\alpha$ =7 deg, flow separation takes place at about x/c=0.30 and a recirculation bubble extending beyond the airfoil trailing edge is found, according to Ref. [15] (see flow sketch). At  $\alpha$ =10 deg, present results differ from those of Ref. [15].

Additionally, the contours of turbulent viscosity with the presence of streamlines further facilitate understanding of the laminar separation and flow transition phenomenon. Specifically, the presence of the laminar separation bubble followed by the transition to turbulent flow is clearly recognizable.

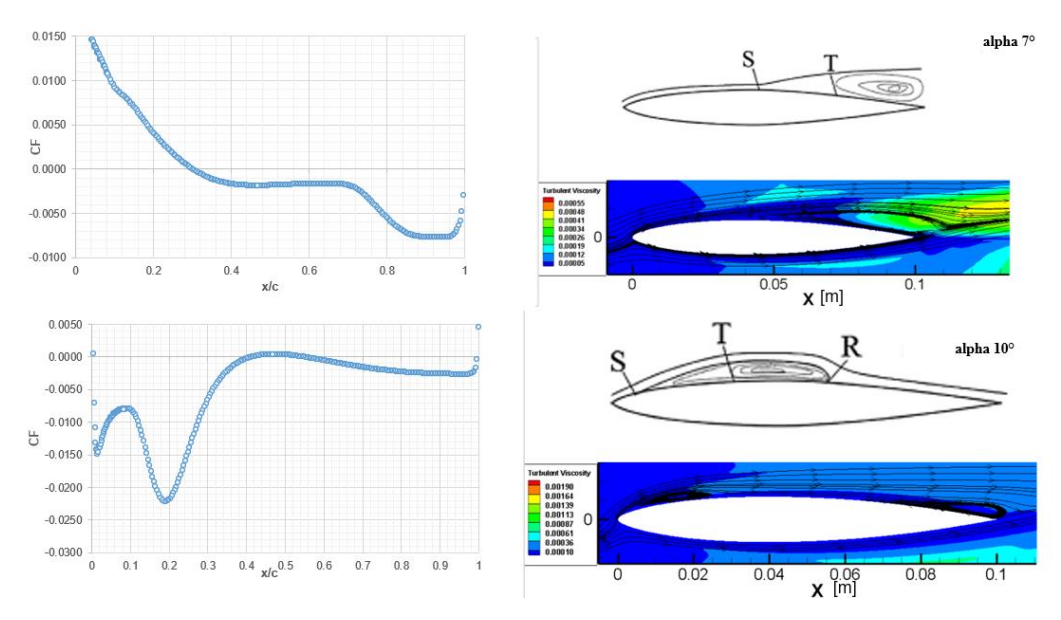


Figure 7 – NACA0012-34. CF and turbulent viscosity [kg/m s] at  $\alpha$ =7°, 10°,  $M_{\infty}$ =0.20 and  $Re_{\infty}$ =11x10³

The current analysis indicates that the  $\kappa$ - $\omega$ - $\gamma$ -Re $_{\Theta}$  turbulence model under examination can replicate the separation phenomenology rather well, albeit with some differences, pertaining to the reattachment phenomenology, like those found for  $\alpha$ =10 deg. These differences may be attributed to the inherent complexity of the case, given the flow at Reynolds number 11x10³, and the potential influence of three-dimensional effects.

### 5.3 NACA0012-34 airfoil at Re $\infty$ =11×10<sup>3</sup> and M $\infty$ =0.60

Lift coefficients versus  $\alpha$  of NACA0012-34 airfoil at  $M_\infty$ =0.60 and  $Re_\infty$ =11x10³ are provided in Figure 8. In this figure, results comparison among ANSYS-FLUENT, SU2, and WT data is shown [15]. As one sees, a quite satisfying comparison exists between ANSYS-FLUENT and WT results, while less accurate lift coefficients are obtained with SU2.

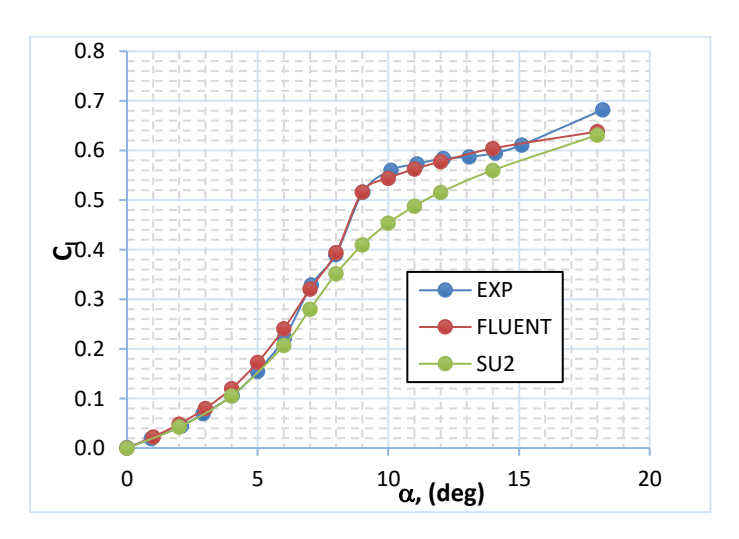


Figure 8 –  $C_1$  vs  $\alpha$ . NACA0012-34 airfoil at  $M_{\infty}$ =0.60 and  $Re_{\infty}$ =11x10<sup>3</sup>

Flowfield results point out that at Mach 0.6, akin to the experimental results, there is no reattachment of the flow post-separation at any angle of attack  $\alpha$ , see for instance results for  $\alpha$ =7° and 10° provided in Figure 9. These results align consistently with the WT data [15].

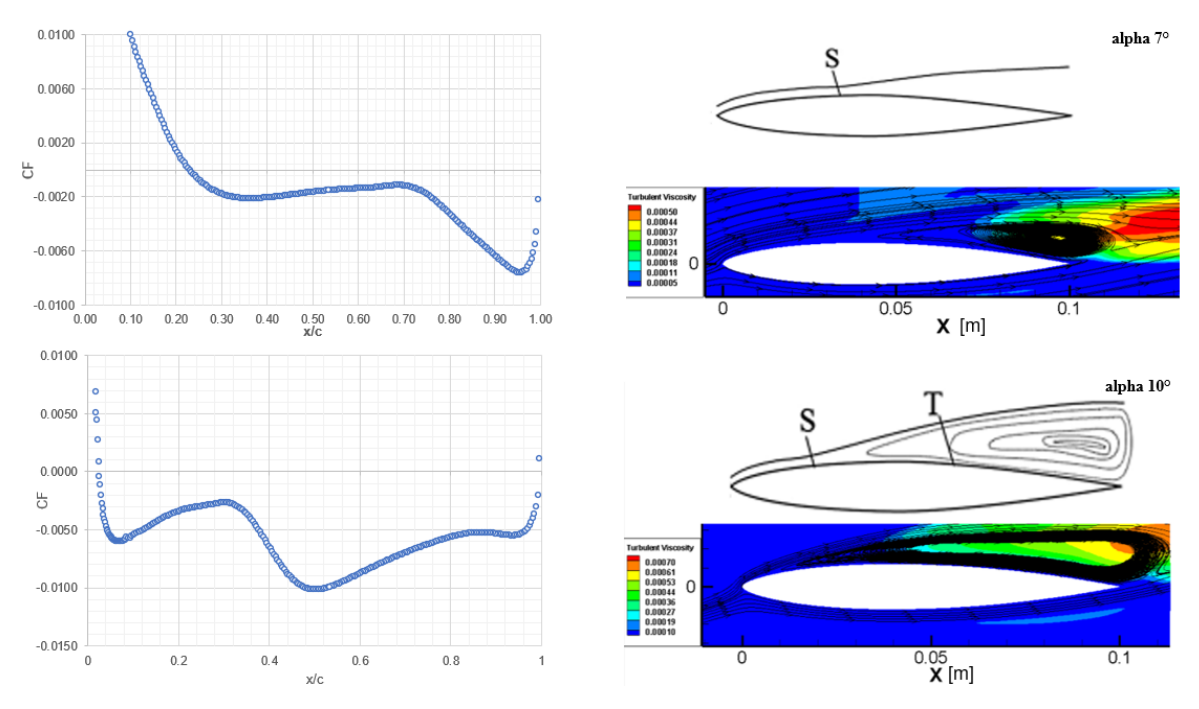


Figure 9 – NACA0012-34. CF and turbulent viscosity [kg/m s] at  $\alpha$ =7°, 10°, M $_{\infty}$ =0.60 and Re $_{\infty}$ =11x10³

# 5.4 NACA0012-34, results comparison between M<sub>∞</sub>=0.20 and M<sub>∞</sub>=0.60

Comparing results for  $M_{\infty}$ =0.20 and 0.60 it is possible to appreciate the effects of flow compressibility on NACA0012-34 aerodynamics, as summarized in Figure 10.

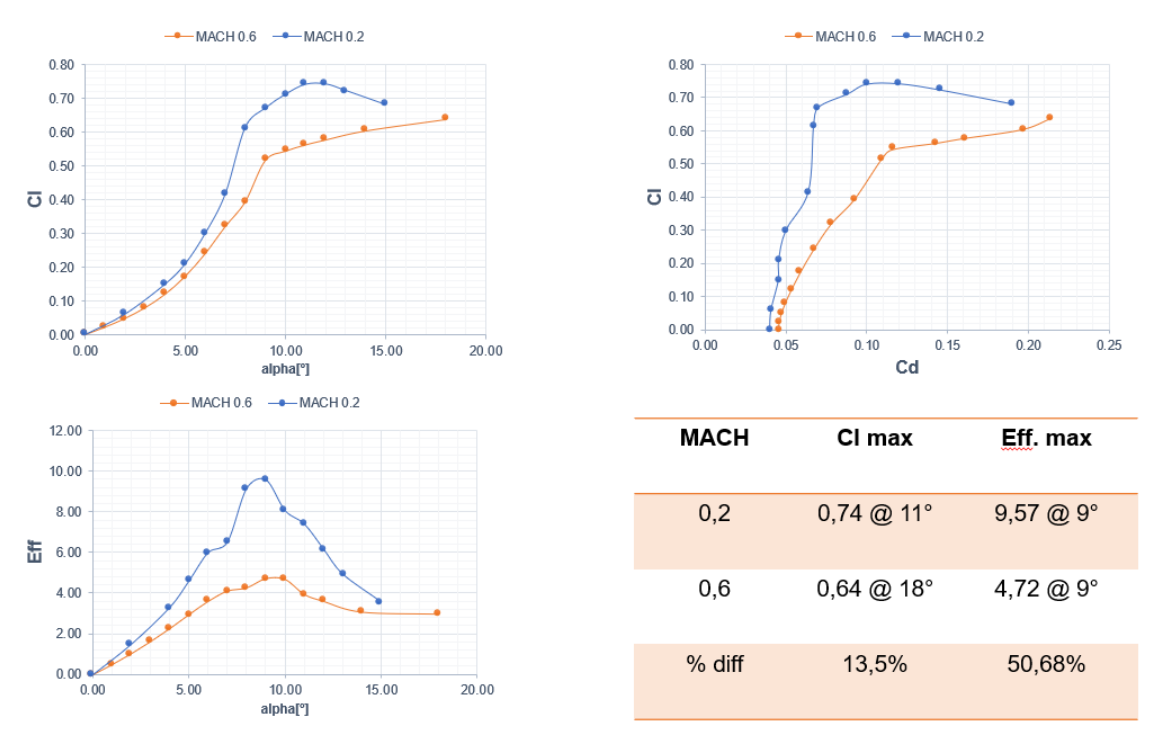


Figure 10 – NACA0012-34 aerodynamics at  $M_{\infty}$ =0.20,  $M_{\infty}$ =0.60, and  $Re_{\infty}$ =11x10<sup>3</sup>

This figure points out that the increase in Mach number determines a progressive decrease in lift coefficient and increase in drag, thus determining a markedly loss in aerodynamic efficiency. This confirms, as pointed out in Reff. [14] [15], that the lift coefficient decreases as Mach number increases.

This suggests that the classical compressibility rules such as Prandtl-Glauert do not apply at low Reynolds flow conditions.

# 5.5 ISHII airfoil at Re $_{\infty}$ =23×10<sup>3</sup> and M $_{\infty}$ =0.20

Figure 11 illustrates lift and drag coefficients curves of the ISHII wing section at  $Re_\infty = 23 \times 10^3$  and  $M_\infty = 0.20$  obtained from CFD and WT test campaigns [14]. As one can see, results comparison points out a rather good agreement between numerical and experimental data, thus confirming the reliability of the present numerical results for  $C_I$ . Regarding the drag coefficient, it is showed a discrepancy attributable to flow three-dimensional effects present in the WT results, see Ref. [14].

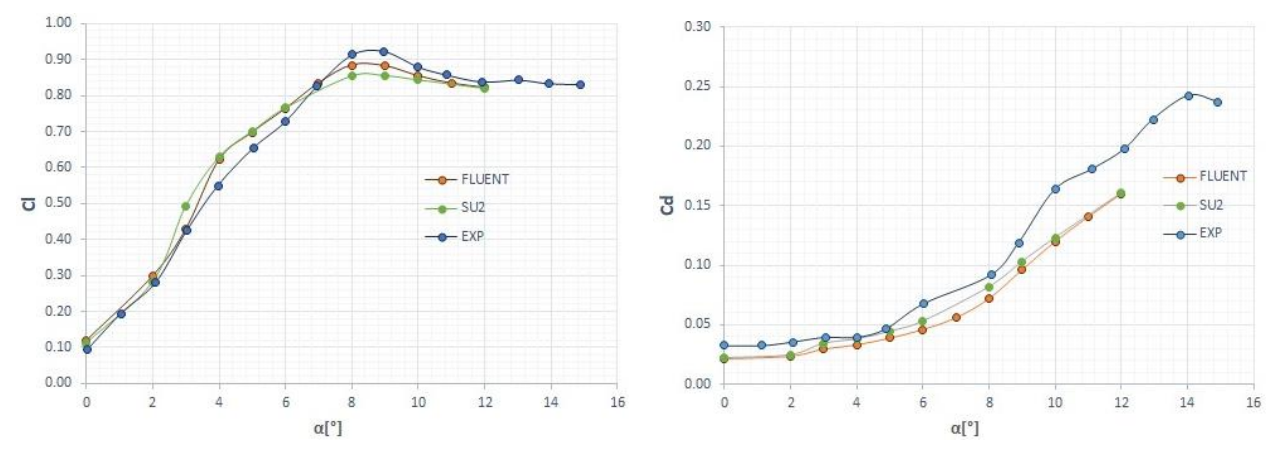


Figure 11 – ISHII airfoil aerodynamics at M<sub>∞</sub>=0.20 and Re<sub>∞</sub>=23x10<sup>3</sup>

Numerical results for skin friction coefficient and turbulent viscosity at  $\alpha$ =6°and  $\alpha$ =9°are shown in Figure 12. The extensions of the laminar separation bubble in this flow conditions are clearly recognizable from the CF profiles, while contours of the eddy viscosity allow further understanding the phenomenon of laminar separation and flow transition.

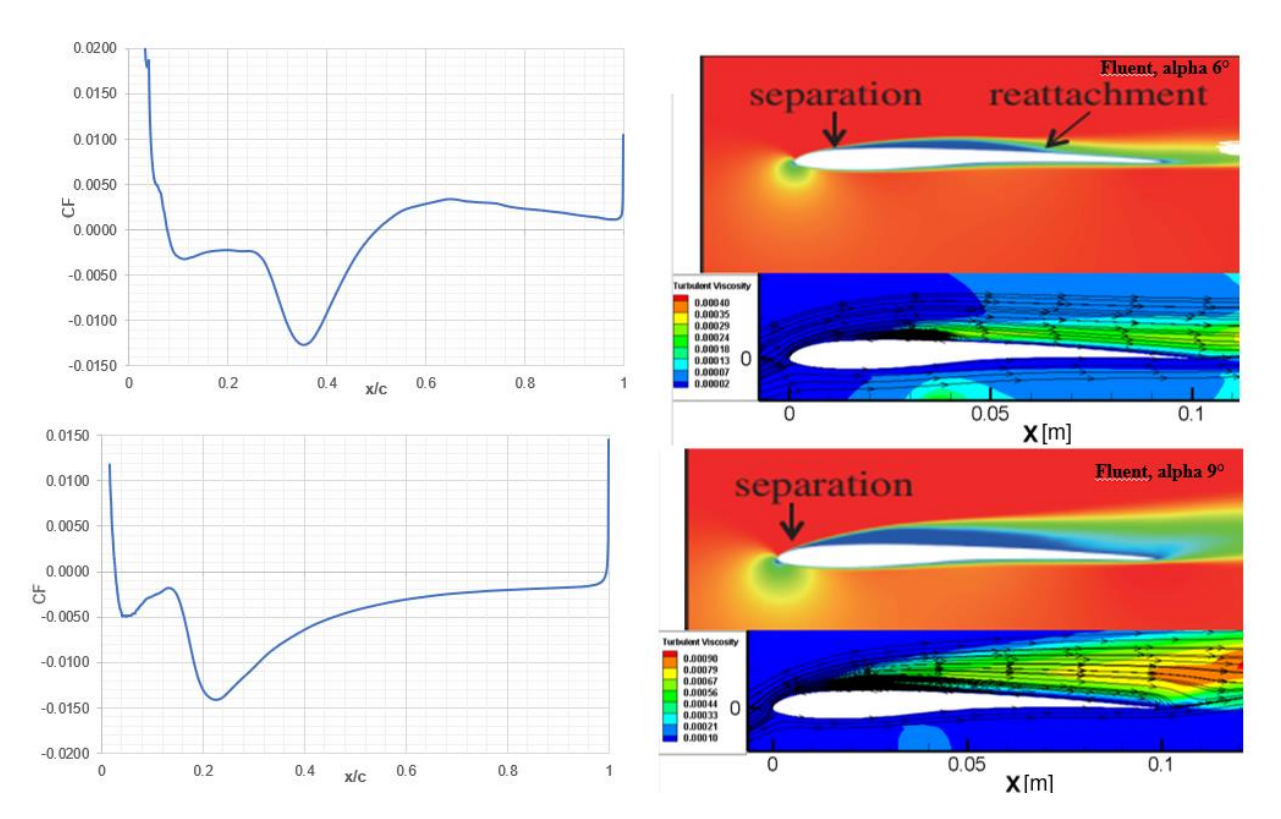


Figure 12 – ISHII airfoil. CF and turbulent viscosity [kg/m s] at α=6°, 9°, M<sub>∞</sub>=0.20 and Re<sub>∞</sub>=23x10<sup>3</sup>

### 5.6 EPPLER-387 airfoil at Re $_{\infty}$ =60×10<sup>3</sup> and M $_{\infty}$ =0.05

Results comparison among XFoil, CFD, and WT data for the E387 airfoil is provided in Figure 13. Airfoil aerodynamics in terms of  $C_1$  versus  $\alpha$  (left side) and drag polar (right side) is recognized [11].

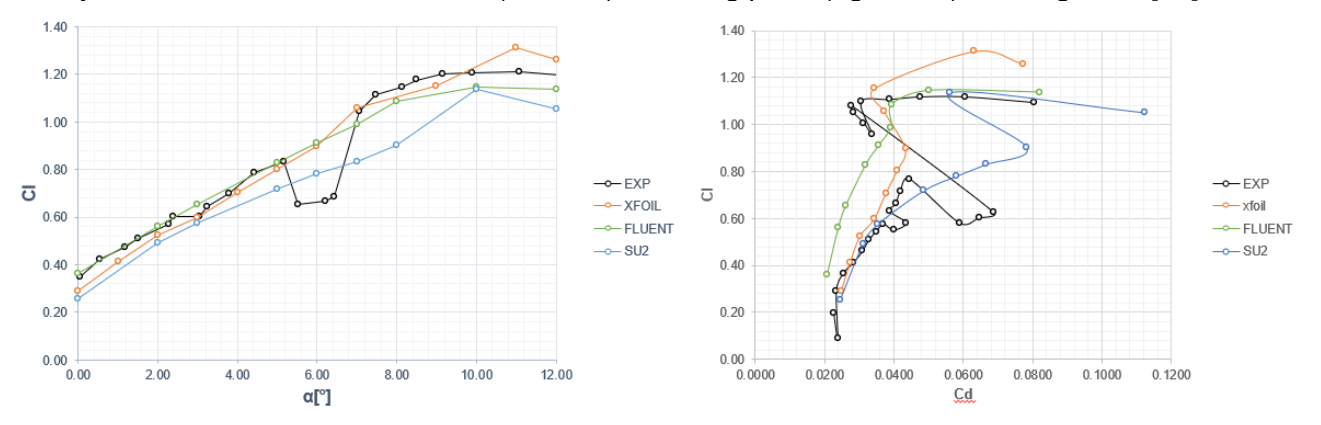


Figure 13 – E387 airfoil aerodynamics at M<sub>∞</sub>=0.05 and Re<sub>∞</sub>=60x10<sup>3</sup>

Lift coefficients provided by XFoil and ANSYS-FLUENT agree rather well with WT data except at approximately  $\alpha$ =6 deg, where measurements record the effects of a strong flow separation not envisaged in the CFD simulations [11]. Results comparison highlights that less accurate seem the results obtained by SU2, especially for attitudes close to  $\alpha$ =8 deg, as also confirmed by Figure 14. This figure shows CF profiles and contours of turbulent viscosity computed by ANSYS-FLUENT and SU2. As one can see, both SU2 and ANSYS-FLUENT foreseen flow separation at about 20% of airfoil chord, but SU2 solution does not exhibit flow reattachment. This discrepancy in results stems from the use of different freestream turbulence conditions for the two solvers. This difference underscores the need for meticulous and critical evaluation of the results obtained across various CFD platforms, highlighting how the unique characteristics of the implemented algorithms can have a significant impact on the accurate prediction of fluid dynamic phenomena.

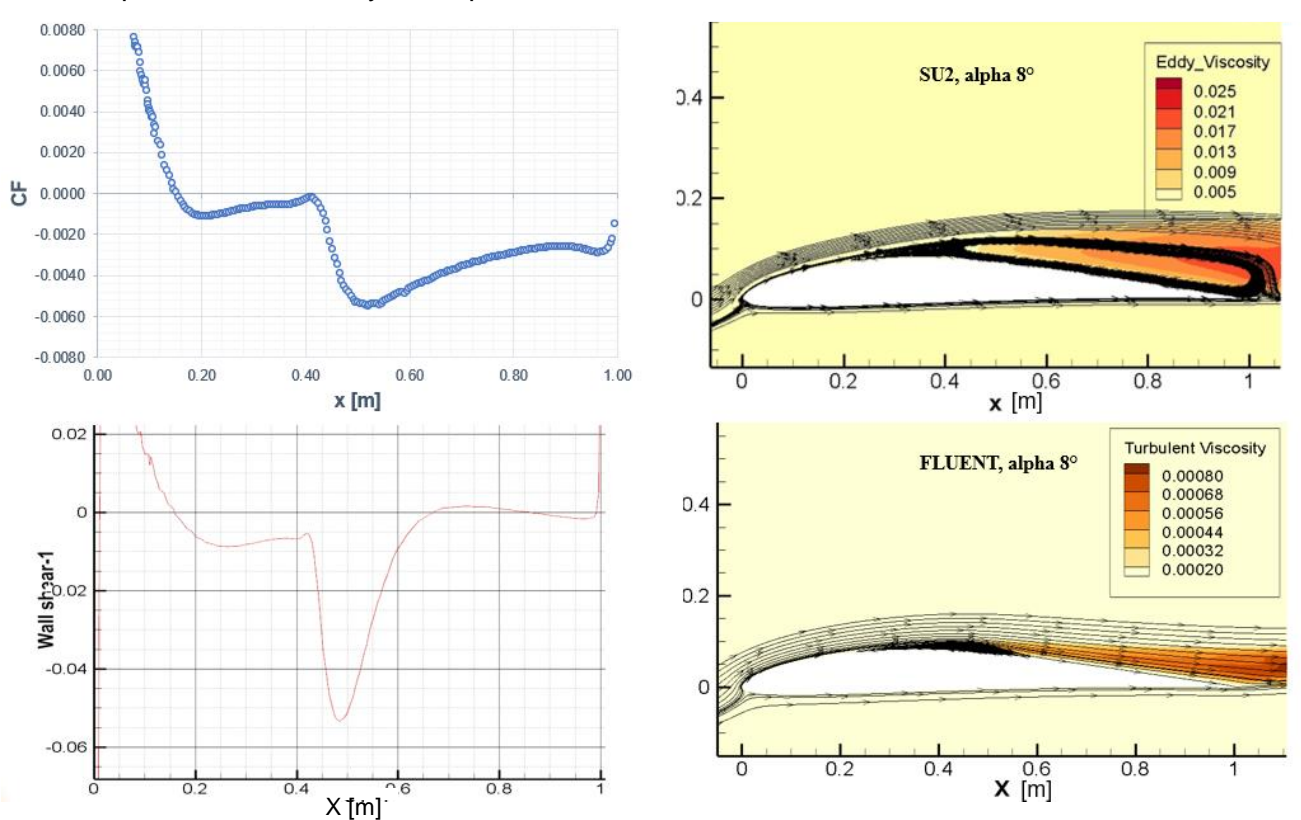


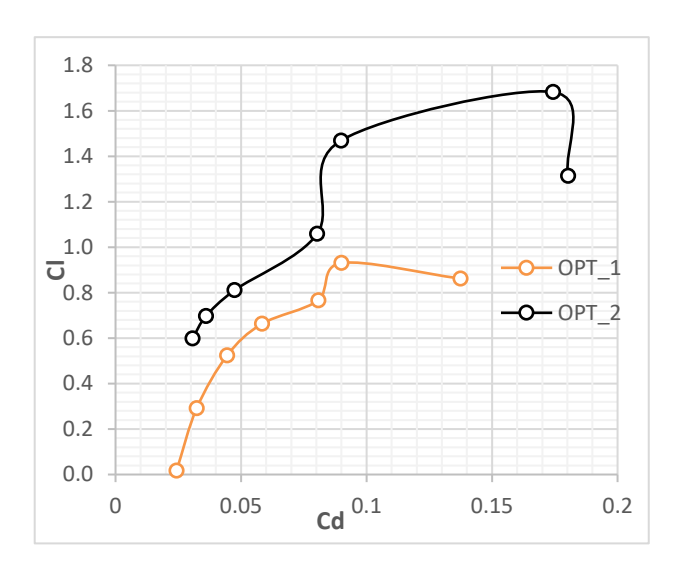
Figure 14 – E387 airfoil. Wall shear (CF) and turbulent viscosity [kg/m s] at  $\alpha$ =8°,  $M_{\infty}$ =0.05 and  $Re_{\infty}$ =60x10<sup>3</sup>

# 5.7 OPT 1 and OPT 2 airfoils at Re∞=34×10<sup>3</sup> and M∞=0.05

Numerical investigations are also performed to assess aerodynamics of two in-house developed airfoils, namely OPT-1 and OPT-2, see Figure 1. Those wing sections are obtained throughout a design optimization procedure aimed at maximizing their aerodynamic efficiency [2]. Airfoils aerodynamic performance at  $Re_\infty=34\times10^3$  and  $M_\infty=0.05$  is summarized in both Table 3 and Figure 15. As shown, OPT\_2 airfoil features a better aerodynamics with respect to OPT\_1, thus suggesting that at low Re airfoils with high camber and low thickness are mandatory.

| Airfoil | (L/D) <sub>Max</sub> XFoil | (L/D) <sub>Max</sub> CFD |
|---------|----------------------------|--------------------------|
| OPT_1   | 30.32%@ α= 7°              | 11.77%@ α= 4°            |
| OPT_2   | 35.62%@ α= 7°              | 19.51%@ α= 0°            |

Table 3 OPT\_1 and OPT\_2 results comparison



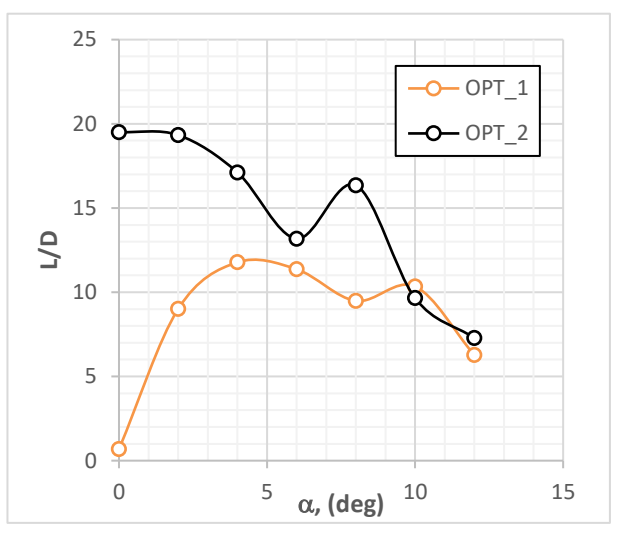


Figure 15 – OPT\_1 O PT\_2 airfoils aerodynamics at  $M_{\infty}$ =0.05 and  $Re_{\infty}$ =34x10<sup>3</sup>

#### 6 TURBULENCE PARAMETER GENERATOR TOOL

One of the primary objectives of this paper is to assess the influence of free-stream turbulence levels on CFD results, with a specific emphasis on devising an effective algorithm for generating such values in scenarios characterized by low Reynolds and Mach numbers. To accomplish this objective, a MATLAB script was developed. The creation of this script required the establishment of a database containing free-stream turbulence values for free flow, which were utilized in all the numerical simulations carried out in the present research effort. The results of these simulations were then compared with experimental data to validate their accuracy. Additionally, the script takes into account also for flow operating conditions and geometric characteristics of airfoil, see Table 1 and Table 2. The MATLAB script was developed as a flexible and interactive tool. It accepts inputs related to the specific geometric characteristics of the airfoil and the desired flow operating conditions. In particular,

- X1=REYNOLDS
- X2=MACH
- X3=MAX CAMBER
- X4=MAX THICKNESS
- X5=ANGLE OF ATTACK

the script requires the following input variables:

This enables precise customization of the free-stream turbulence parameters generation process. After receiving the specified information, the script processes the data and provides the turbulence values to be considered in the CFD simulation. This dynamic approach, involving user interaction and

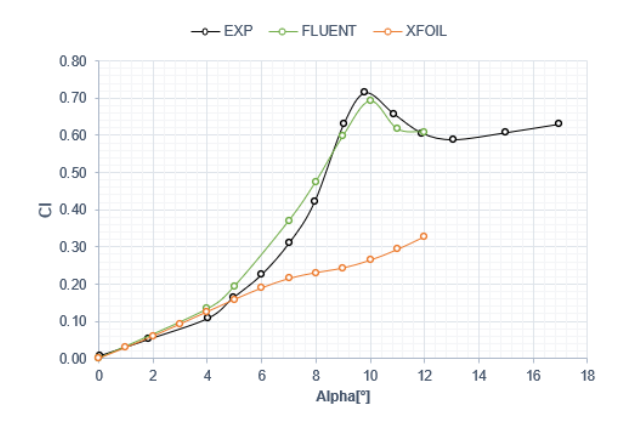
customization of input variables, ensures that the results are tailored to the specific requirements of each simulation. The development of such a versatile and adaptable tool underscores the commitment to finding efficient solutions for generating turbulence parameters, enhancing the precision of CFD analysis and aligning it with the unique conditions of each case study. This analysis led to the generation of two polynomials shown in Eq. (5) and Eq. (6) whose variables are values of k (turbulent kinetic energy) and  $\omega$  (specific dissipation rate).

Turbulent kinetic energy= 
$$-0.00044 * X1 + 195.4024 * X2 + 452.1395 * X3 + 637.3628 * X4 + 1.1905 * X5 - 63.512$$
 (5)

Specific dissipation rate = 
$$-0.093057 * X1 + 1951.8801 * X2 + 5195.5602 * X3 - 110773.9682 * X4 - 147.616 * X5 + 16752.0802$$
 (6)

#### 6.1 Tool validation

The meticulous selection of freestream turbulence parameters played a pivotal role in guaranteeing the success of the RANS simulations. Consequently, the development of a dedicated code capable of estimating these turbulence parameters was imperative to ensure the robustness and accuracy of the simulations. To assess the effectiveness of this code, comprehensive simulations were executed employing the NACA 0012-34 profile at Re=11x10³ and Mach 0.48, with comparison data derived from experimental analysis [15]. The outcomes from these simulations distinctly demonstrate the efficacy of the code in delivering dependable estimates of freestream parameters for inlet turbulence. Numerical results are shown in Figure 16.



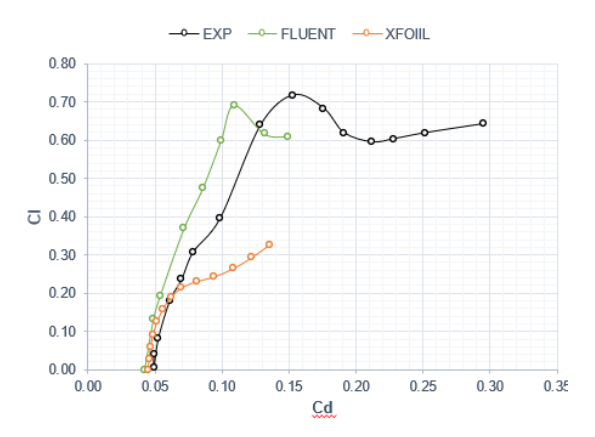


Figure 16 – NACA0012-34 airfoil aerodynamics at M<sub>∞</sub>=0.48 and Re<sub>∞</sub>=11x10<sup>3</sup>

# 7 OPT 3 at $Re_{\infty} = 45 \times 10^{3}$ and $M_{\infty} = 0.15$

Following the comprehensive analysis of the optimized airfoils OPT\_1 and OPT\_2, a third airfoil, denoted as OPT\_3, underwent scrutiny. This airfoil was derived through an optimization process applied to the geometry of OPT\_1, this time targeting a Reynolds number of 45,000, typical for cruise flight in a Martian atmosphere [2] [3]. This systematic approach allows for an exploration of how alterations to the optimized shape of OPT\_1 influence the airfoil's aerodynamic performance under varying operating conditions. The analysis of OPT\_3 introduces an additional layer of detail to the investigations, facilitating an assessment of how the optimized features, initially designed for a specific Reynolds number, respond to different aerodynamic stresses. This sequence of optimized airfoil analyses offers a comprehensive overview of aerodynamic performance, contributing to an enhanced understanding of how geometric changes impact the overall airfoil behavior across diverse examined operating conditions. The analysis of OPT\_3 was performed on a structured two-dimensional grid of 126000 elements having the height of the first cell close to the body equal to 0.38 mm.

The turbulence free-stream conditions for the OPT\_3 simulations were obtained through the MATLAB tool, as discussed in chapter 6.

CFD simulations were conducted by replicating the Martian atmosphere at about 1 km altitude. This atmospheric setting introduces an additional layer of complexity to the simulations, but provides

valuable insights into OPT\_3 performance under realistic flying operational scenarios. Airfoil aerodynamics is provided in Figure 17 and Figure 18.

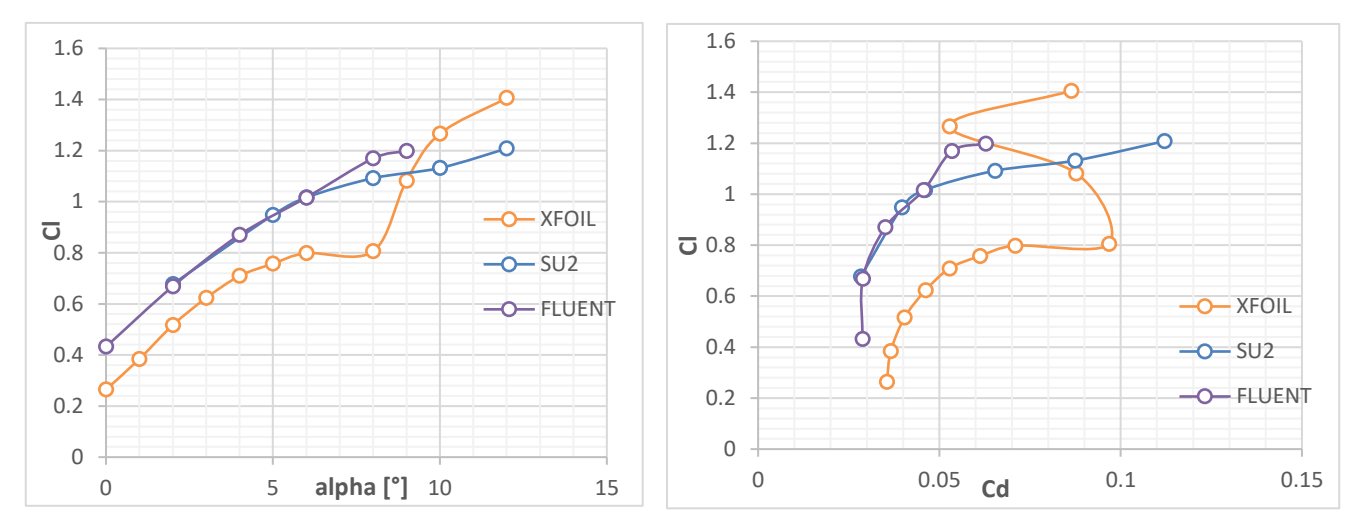


Figure 17 – OPT\_3 airfoil aerodynamics at M<sub>∞</sub>=0.15 and Re<sub>∞</sub>=45x10<sup>3</sup>

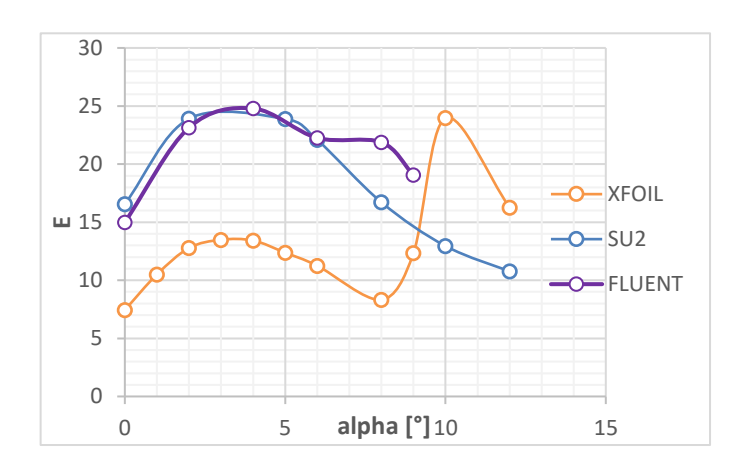


Figure 18 – OPT\_3 airfoil. Lift-to-drag ratio at  $M_{\infty}$ =0.15 and  $Re_{\infty}$ =45x10<sup>3</sup>

It is noteworthy from the aforementioned figures that XFoil underestimates the lift characteristics compared to Fluent and SU2. This discrepancy could be attributed, in addition to the inherent challenges of the analyzed cases, to the limited configuration of the turbulence model employed by XFoil for solving the flow field, as previously observed in other analyses.

The utilization of freestream turbulence values derived from the polynomial has led to several results in terms of aerodynamic efficiency, as shown in Figure 18.

#### 8 Conclusion

In this study, comprehensive aerodynamic analyses were conducted on airfoil profiles under low Reynolds number conditions, aiming to replicate Martian atmospheric conditions. The use of CFD simulations enabled a detailed understanding of fluid dynamic phenomena, such as flow separation and reattachment. The development of a dedicated code to provide information on inlet turbulence conditions for RANS simulations was a crucial step in improving simulation accuracy. This tool contributed to increased precision in aerodynamic predictions, facilitating a better understanding of the fluid dynamic phenomena involved. This study provides a solid foundation for further research in the field of aerodynamics applied to low Reynolds and Mach number conditions, with potential implications for the design of aircraft in non-terrestrial atmospheres. Further investigations are needed to refine profile optimizations and explore additional details of two-dimensional and three-dimensional flow behavior.

Finally, achieved results have shown that the classical compressibility rules such as Prandtl-Glauert do not apply at low Reynolds flow conditions. In fact, the lift coefficient decreases as Mach number

increases.

#### 9 Contact Author Email Address

Giuseppe Pezzella: giuseppe.pezzella@unicampania.it

# 10 Copyright Statement

The authors confirm that they, and/or their company or organization, hold copyright on all of the original material included in this paper. The authors also confirm that they have obtained permission, from the copyright holder of any third part material included in this paper, to publish it as part of their paper. The authors confirm that they give permission, or have obtained permission from the copyright holder of this paper, for the publication and distribution of this paper as part of the ICAS proceedings or as individual off-prints from the proceedings.

#### 11 REFERENCES

- [1] J. Morgado, R. Vizinho, M. A. Silvestre e J. C. Páscoa, «Xfoil vs cdf performance predictions for high lift low reynolds number airfoils,» *Aerospace Science and Technology*, vol. 52, pp. 207-214, 2016.
- [2] A. Aprovitola, L. Iuspa, G. Pezzella e A. Viviani, «Aerodynamic Optimization for Airfoil Shape for atmospheric flight on Mars Planet,» *Acta Astronautica* 212, pp. 580-594, 2023.
- [3] A. Aprovitola, L. Iuspa, G. Pezzella e A. Viviani, «Flows past airfoils for the low-Reynolds number conditions of flying in Martian atmosphere,» *Acta Astronautica 221*, pp. 94-107, 2024.
- [4] M. Hassanalian, D. Rice e A. Abdelkefi, «Evolution of space drones for planetary exploration: A review,» *Progress in Aerospace Sciences*, vol. 97, pp. 61-105, 2018.
- [5] S. Rodriguez, «Applied Computational Fluid Dynamics and Turbulence Modeling.,» *Springer Cham.* 978-3-030-28693-4., Published: 06 January 2021.
- [6] P. Catalano e R. Tognaccini, «RANS analysis of the low-Reynolds number flow around the SD7003 airfoil,» *Aerospace science and technology,* vol. 15, 2011.
- [7] M. S. Selig e B. D. McGranahan, «Wind Tunnel Aerodynamic Tests of Six Airfoils for Use on Small Wind Turbines,» in *42nd AIAA Aerospace Sciences Meeting and Exhibit*, American Institute of Aeronautics and Astronautics, 2004.
- [8] D. A. Olson, A. W. Katz, A. M. Naguib, M. M. Koochesfahani, D. P. Rizzetta e M. R. Visbal, «An Investigation of the effect of Freestream Turbulence on the Laminar Separation Bubble on an SD7003 Airfoil,» in *49th AIAA Aerospace Sciences Meeting including the New Horizons Forum and Aerospace Exposition*, Orlando, Florida, 2011.
- [9] J. Winslow, H. Otsuka, B. Govindara e I. Chopra, «Basic Understanding of Airfoil Characteristics at Low Reynolds Numbers (10^4–10^5), » *JOURNAL OF AIRCRAFT*, vol. 55, n. 3, pp. 1050-1061, 2018.
- [10] G. Barbato, G. Pezzella e A. Viviani, "Preliminary Design of a Fixed-Wing Drone for Mars Exploration Activities," in 34th Congress of the International Council of the Aeronautical Sciences (ICAS), Florence, Italy, 2024.
- [11] R. J. McGhee e B. S. Walker, «Experimental results for the E387 airfoil at Low-Reynolds number in the Langley Low-Turbulence Pressure tunnel,» *NASA tecnical memorandum 4062*, 1988.
- [12] Ansys, «Fluent,» [Online]. Available: https://www.ansys.com/products/fluids/ansys-fluent.
- [13] R. B. Langtry e F. R. Menter, «Correlation-based transition modelling for unstructured parallelized computational fluid dynamics codes,» *AIAA Journal*, vol. 47, n. 12, p. 2894–2906, 2009.
- [14] M. Anyoji, T. Nonomura, H. Aono, A. Oyama e K. Fujii, «Computational and Experimental Analysis of a High-Performance Airfoil under Low-Reynolds-Number-Flow Condition,» *Journal of Aircraft*, vol. 51, n. 6, pp. 1864-1872, 2014.
- [15] M. Anyoji, D. Numata, H. Nagai e K. Asai, «Effects of Mach Number and Specific Heat Ratio on Low-Reynolds-Number Airfoil Flows,» *AIAA Journal*, vol. 53, n. 6, pp. 1640-1654, 2015.